Optimal Length Scales Emerging from Shear Load Transfer in Natural Materials: Application to Carbon-Based Nanocomposite Design

Xiaoding Wei, Mohammad Naraghi, and Horacio D. Espinosa*

Department of Mechanical Engineering, Northwestern University, 2145 Sheridan Road, Evanston, Illinois 60208-3111, United States

ABSTRACT

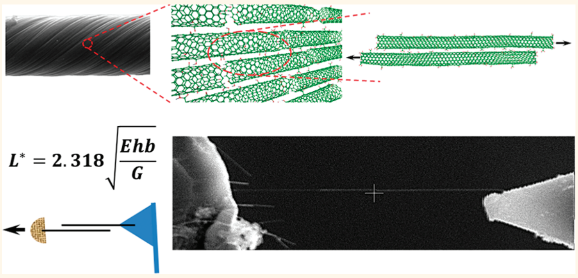

Numerous theoretical and experimental studies on various species of natural composites, such as nacre in abalone shells, collagen fibrils in tendon, and spider silk fibers, have been pursued to provide insight into the synthesis of novel bioinspired high-performance composites. However, a direct link between the mechanical properties of the constituents and the various geometric features and hierarchies remains to be fully established. In this paper, we explore a common denominator leading to the outstanding balance between strength and toughness in natural composite materials. We present an analytical model to link the mechanical properties of constituents, their geometric arrangement, and the chemistries used in their lateral interactions. Key critical overlap length scales between adjacent reinforcement constituents, which directly control strength and toughness of composite materials, emerge from the analysis. When these length scales are computed for three natural materials—nacre, collagen molecules, and spider silk fibers—very good agreement is found as compared with experimental measurements. The model was then used to interpret load transfer capabilities in synthetic carbon-based materials through parametrization of *in situ* SEM shear experiments on overlapping multiwall carbon nanotubes.

KEYWORDS: natural materials · toughness · nanocomposites · shear load transfer

Natural and biological materials are found to exhibit an outstanding balance of stiffness, strength, and fracture toughness. In contrast, synthetic engineering materials typically do not achieve such a balance. For example, as shown in Figure 1, synthetic materials sacrifice toughness as their stiffness is improved, and *vice versa*.[1] In the past two decades, significant efforts have been undertaken to understand the secret of natural materials,[2] which achieve high stiffness and toughness from relatively weak constituents and chemical bonds (*e.g.*, hydrogen bonds).[3,4]

Commonly found in nature, mollusk shells are an excellent example of high-performance biological composites.[5,6] For instance, abalone shell is composed of about 95% aragonite, a brittle mineral. However, it exhibits a toughness about 3000 times higher than aragonite.[6−10] Examining the hierarchical architecture of red abalone reveals that stacks of 8 μm long and 0.5 μm thick aragonite tiles are overlapped and connected by a 20−30 nm thick layer of organic material (see Figure 2a). The average overlap length is approximately 1.6 μm.[11,12] Studies suggest that this "brick-and-mortar" structure allows large sliding deformation of tablets and suppresses the strain localization and crack propagation in the brittle aragonite tiles.[6,13,14] The overlap length is found to be critical in the load transfer mechanism. Gao *et al.*[15] estimated a critical overlap length using Griffith's fracture criterion. They suggested that the optimal aspect ratio of tablets in a biological composite is σ_f/τ_f, where σ_f and τ_f are the tensile and shear strength of the tablet and matrix materials, respectively. However, the elastic properties of each constituent, which emerge in the model presented here, were not accounted for in ref 15. Given that nacre presents a three-dimensional tablet organization, it is impossible to achieve a uniform overlap length in all in-plane directions. Therefore, various deformation mechanisms have been proposed to explain the extra toughening observed in this material. Wang *et al.*[16] and Evans *et al.*[17] claimed that

* Address correspondence to espinosa@northwestern.edu.

Received for review November 19, 2011 and accepted February 8, 2012.

10.1021/nn204506d

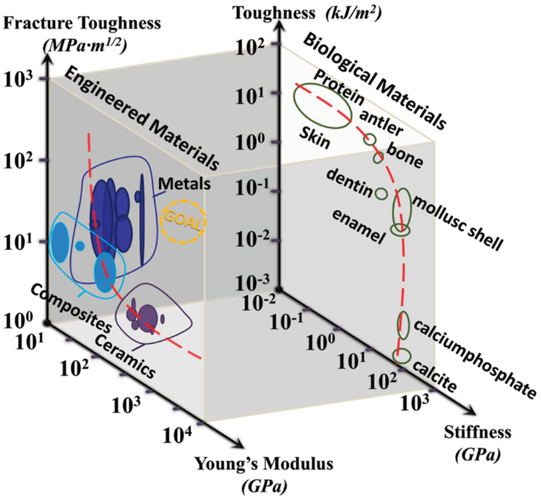

Figure 1. Comparison of performance of engineered and biological materials in the stiffness–toughness domain. Stiffness *vs* toughness trend for common synthetic materials (plot adapted from Ashby *et al.*[1]) follows the dashed red curve, exhibiting strong reduction in fracture toughness when stiffness is improved. Stiffness *vs* toughness trend for common biological materials (plot adapted from Fratzl *et al.*[2]) shows a "reinforcing" combination of organic toughness and inorganic stiffness. The "goal" region, in the engineering materials plot, represents materials with high stiffness and toughness that may be synthesized through bioinspired design.

nanoasperities on the tablet surface may interact in shear and act as a source of interface strengthening. Song *et al.*[18] proposed that the aragonite bridges at the interface act as reinforcements during tablet sliding. Furthermore, Meyers *et al.*[19] claimed that at large sliding deformation, the broken aragonite bridges re-enter in contact and relock the tablets. Katti *et al.*[20] claimed that the interlocking of adjacent mineral platelets acts as the source of strengthening of nacre. By contrast, Espinosa *et al.*[11,12] showed that diffusive tablet sliding is a result of tablet interface hardening from the waviness of the tablet surfaces. Their understanding emerged from a multiscale experimentation approach and detailed micromechanical modeling.

Tendon is another perfect example of a biomaterial that exhibits remarkable toughness. In this case, unlike the sheet structure in abalone shell, tendon takes the form of a hierarchical fiber, the structure of which is shown in Figure 2b. Tendon fibers consist of aligned collagen fibrils, which are based on tropocollagen molecules. An individual tropocollagen molecule, which is triple-helical protein chain, has a length of about 300 nm and a diameter of about 1.23 nm.[21−24] As indicated in Figure 2b, neighboring molecules are shifted by a distance $D = 67$ nm in the axial direction. The gap, G, between tropocollagen molecules is approximately $0.6D = 40$ nm; thus, the overlap length, O, equals $0.4D = 27$ nm. Therefore, similar to mollusk shells, tendon can be thought of as a "brick-and-mortar" structure, although in a smaller length scale (tropocollagen molecules *vs* aragonite tiles). These collagen fibrils assemble into fascicles, which in turn assemble into the tendon fiber. Tendon has an elastic modulus on the order of 1 GPa, a tensile strength of about several hundred MPa, and a fracture strain up to 100%.[25−27] Buehler *et al.*[28,29] performed extensive atomistic calculations on individual tropocollagen molecules and collagen fibrils and found that the hierarchical architecture of collagen fibrils optimizes its mechanical performance.

Spider silk is another natural fibrous material that has attracted a lot of attention due to its high strength and great extensibility. The elastic modulus of spider silk is on the order of 5 GPa, and the strength is about 1.5 GPa.[30] Figure 2c shows the hierarchical structure of spider silk, starting with small crystals interconnected by an amorphous matrix leading to microfibrils. The antiparallel β-sheet crystal, the lowest level element in spider silk, is believed to play a key role in its unique mechanical properties.[31] The β-sheet crystals are bonded by hydrogen bonds (H-bonds) and typically have dimensions of a few nanometers. Atomistic calculations by Keten *et al.*[31,32] have shown that the dimensions of the β-sheet crystals optimize its toughness. In fact, the study suggests that crystal dimensions of 1−2 nm by 2−4 nm are needed to deform hydrogen bonds in shear rather than in tension.

Since carbon-based materials, such as carbon nanotubes (CNTs) and graphene, have been experimentally proved to have excellent mechanical properties, such as high elastic modulus and ultimate strength,[33,34] researchers have been exploring the possibilities of utilizing them to fabricate bioinspired high-performance nanocomposites.[35−40] However, the theoretical studies on natural materials described above either explain the optimization of mechanical properties of only a specific biomaterial or are difficult to apply to general cases because the mechanical properties in the model are hard to characterize. Therefore, developing a universal theory that can provide guidelines to general composite design is essential. Here we present a continuum analysis and introduce a general model that explains the optimization of hierarchical architectures observed in natural composites. In particular the model predicts characteristic overlap lengths that optimize the mechanical performance in a variety of natural materials (namely, abalone shell, tendon, and spider silk) with very different geometric structures and at a range of different length scales. The predicted overlap lengths are found to be in very good agreement with those found to form by nature, demonstrating its general applicability to both sheet and fibrous materials. In the case of the natural fiber materials, the model is demonstrated to apply across length scales, predicting overlap lengths on the submicrometer scale for collagen fibrils and on the nanometer scale for β-sheet stacking in spider silks. The bioinspired

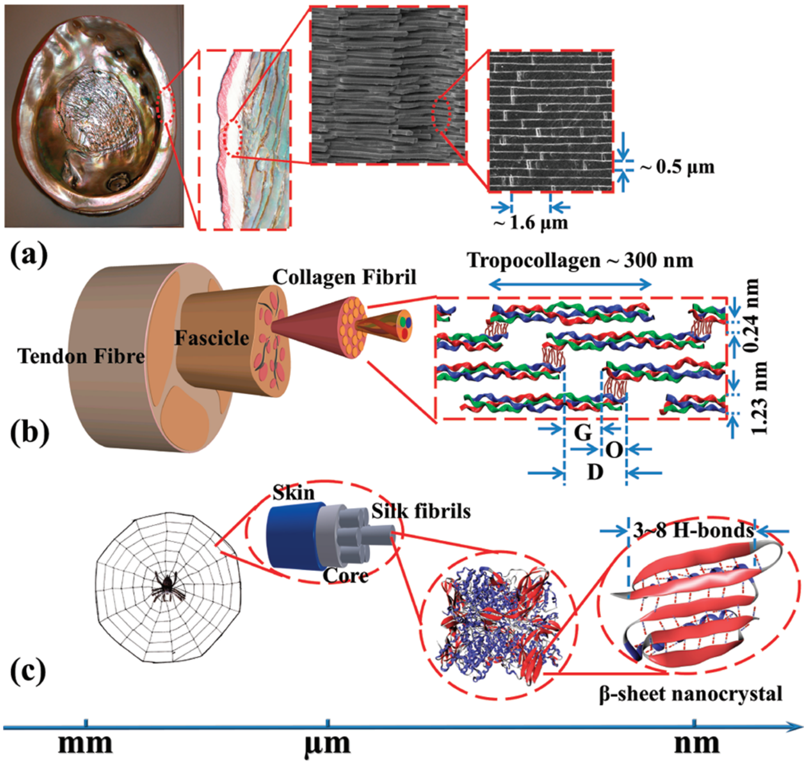

Figure 2. Hierarchical structures of three typical natural composites: (a) nacre shell, (b) tendon, and (c) spider silk, scaling from micrometer down to nanometer.

continuum model is then applied on the two bare carbon nanotube shear test as a basic study of the loading transfer capability inside pristine carbon nanotube fibrils.

CONTINUUM MODEL

The continuum analysis of a biological composite is performed on the simplified 2D unit cell shown in Figure 3, by means of the well-known "shear lag model".[41] Two tablets are connected by the matrix material with overlap length L. Due to periodicity in the thickness direction, we define b as half the tablet width. In the model, h is the matrix thickness. A tensile normal stress, σ_0, is applied at the right end of the top tablet, and the left end of the bottom tablet is fixed in the axial direction, but it is free to deform in the lateral direction. The left end of the top tablet and the right end of the bottom tablet are traction-free and free to move. Therefore, the unit cell simulates the load transfer mechanism through shear in the overlapped region in common biological composites.

Elastic Regime. Given the elastic modulus of the tablet (or fibril), E, the shear modulus of the matrix, G, the tensile strength of the tablet, σ_f, and the shear strength of the matrix, τ_f, the mechanical response of the unit cell shown in Figure 3 can be solved in the linear elastic regime. Force equilibrium of the unit cell requires

$$\tau(x) = b\frac{d\sigma_1(x)}{dx} = -b\frac{d\sigma_2(x)}{dx} \qquad (1)$$

where $\tau(x)$ is the shear stress in the matrix along the overlapped region and $\sigma_1(x)$ and $\sigma_2(x)$ are the axial stresses along the top and bottom tablets, respectively. As h is small, the matrix is in a pure shear;that is, $\tau(x) = G\gamma(x)$, where $\gamma(x) \equiv [u_1(x) - u_2(x)]/h$ is the shear strain and $u_1(x)$ and $u_2(x)$ are the displacements of the top and bottom tablets, respectively. When the tablets deform elastically, the gradient of the shear stress equals

$$\frac{d\tau}{dx} = \frac{G}{h}\left(\frac{du_1}{dx} - \frac{du_2}{dx}\right) = \frac{G}{Eh}(\sigma_1 - \sigma_2) \qquad (2)$$

where du_1/dx and du_2/dx are the definitions of the axial strains along the top and bottom tablets, respectively. Combining eqs 1 and 2 yields the ordinary differential equations:

$$\begin{cases} \dfrac{d^2\sigma_1}{dx^2} = \dfrac{G}{Ehb}(\sigma_1 - \sigma_2) \\ \dfrac{d^2\sigma_2}{dx^2} = \dfrac{G}{Ehb}(\sigma_2 - \sigma_1) \end{cases} \qquad (3)$$

with the boundary conditions given as

$$\begin{cases} \sigma_1(0) = 0, \quad \sigma_1(L) = \sigma_0 \\ \sigma_2(0) = \sigma_0, \quad \sigma_2(L) = 0 \end{cases} \qquad (4)$$

The solution to eqs 3 and 4 is

$$\sigma_1(x) = \frac{\sigma_0}{\sinh\left(\frac{\lambda L}{2}\right)}\sinh\left(\frac{\lambda x}{2}\right)\cosh\left(\frac{\lambda(L-x)}{2}\right)$$
$$\sigma_2(x) = \sigma_1(L-x) = \frac{\sigma_0}{\sinh\left(\frac{\lambda L}{2}\right)}\cosh\left(\frac{\lambda x}{2}\right)\sinh\left(\frac{\lambda(L-x)}{2}\right) \qquad (5)$$

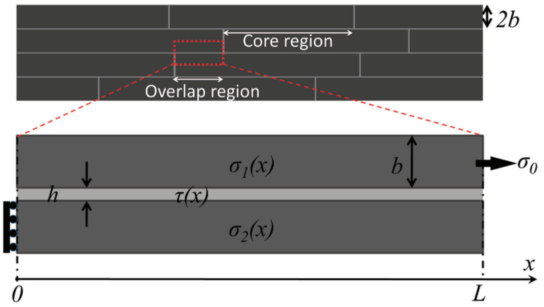

Figure 3. Schematic of 2D unit cell used in the composite continuum model simplified from the architecture of the nacre shell.

where $\lambda = ((2G)/(Ehb))^{1/2}$. Applying eq 1, the solution of the shear stress distribution can be expressed as

$$\tau(x) = \frac{\sigma_0 b\lambda}{2\sinh\left(\frac{\lambda L}{2}\right)}\cosh\left(\lambda\left(x - \frac{L}{2}\right)\right) \qquad (6)$$

By integrating eq 5 and applying the boundary conditions, the displacement fields in the top and bottom tablets are obtained,

$$\begin{aligned} u_1(x) &= \frac{\sigma_0}{2\lambda E}\left\{\lambda x + [1+\cosh(\lambda x)]\coth\left(\frac{\lambda L}{2}\right) - \sinh(\lambda x)\right\} \\ u_2(x) &= \frac{\sigma_0}{2\lambda E}\left\{\lambda x + \sinh(\lambda x) + [1 - \cosh(\lambda x)]\coth\left(\frac{\lambda L}{2}\right)\right\} \end{aligned} \qquad (7)$$

Hence, the effective strain, ε_{eff}, and the effective stress, σ_{eff}, of the composite are

$$\begin{aligned} \varepsilon_{\text{eff}} &\equiv \frac{u_1(x = L)}{L} = \frac{\sigma_0}{2\,\lambda EL}\left[\lambda L + 2\coth\left(\frac{\lambda L}{2}\right)\right] \\ \sigma_{\text{eff}} &= \sigma_0\left(\frac{b}{2b+h}\right) \end{aligned} \qquad (8)$$

Thus, the effective elastic modulus of the composites is given by

$$E_{\text{eff}} \equiv \frac{\sigma_{\text{eff}}}{\varepsilon_{\text{eff}}} = \frac{2E\lambda bL}{(2b+h)\left[\lambda L + 2\coth\left(\frac{\lambda L}{2}\right)\right]} \qquad (9)$$

The elastic solutions presented by eqs 5, 6, and 7 are the same as the well-known "shear-lag model".[41] Figure 4 show a typical distribution of the shear stress and tensile stress along the overlapped length. The shear stress maximizes at both ends and decreases exponentially toward the center. Therefore, for a large overlap length, the composite becomes stiff according to eq 9, but the efficiency of the shear transfer drops, as a major portion of the overlapped region does not carry much shear load. Since the shear transfer mechanism is the key to understanding the mechanical properties of composites, it is important to quantitatively evaluate shear transfer efficiency. Here the elastic strain energy density is used to assess the shear transfer efficiency. From eqs 8 and 6 plus the elastic limit condition $\tau(x = 0) = \tau(x = L) = \tau_f$, the elastic strain energy density of the unit cell can be expressed as

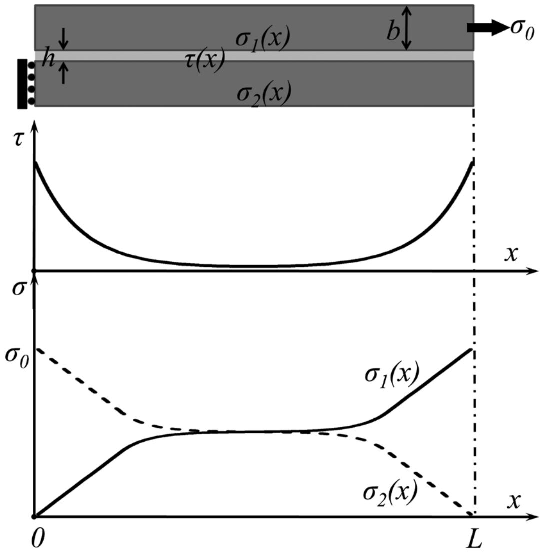

Figure 4. Typical distribution of shear stress and tensile stress in the unit cell within the linear elastic regime.

$$\begin{aligned} w_{\text{el}} &= \frac{{\tau_f}^2}{G}\frac{h}{2b+h}\left[\tanh\left(\frac{\lambda L}{2}\right)\left(\frac{1}{2}\tanh\left(\frac{\lambda L}{2}\right) + \frac{1}{\lambda L}\right)\right] \\ &= \frac{{\tau_f}^2}{G}\frac{h}{2b+h}f(\lambda L) \end{aligned} \qquad (10)$$

where

$$f(\lambda L) = \tanh\left(\frac{\lambda L}{2}\right)\left(\frac{1}{2}\tanh\left(\frac{\lambda L}{2}\right) + \frac{1}{\lambda L}\right) \qquad (11)$$

Equation 10 suggests that when the elastic properties of the tablet and matrix, *i.e.*, E and G, are known and the transverse dimensions of the composite, b and h, are fixed, the elastic strain energy density is a function of L. Therefore, to maximize the elastic strain energy density, one has to maximize $f(\lambda L)$. Solving eq 11 numerically suggests that $f(\lambda L)$ has a maximum at $\lambda L \approx 3.28$, *i.e.*, when the overlap length equals

$$L^* \approx 2.318\sqrt{\frac{Ebh}{G}} \qquad (12)$$

We note that Chen *et al.*[42] reported a similar solution by a dimensional argument, but without a constant of 2.318 as presented in eq 12. This characteristic overlap length, L^*, derived in this study, results from a closed form solution. Furthermore, it has the physical meaning at which the unit cell maximizes its elastic strain energy density (*i.e.*, the shear transfer efficiency).

Plastic Regime for Highly Ductile Matrix. As matrix materials in biocomposites usually show extraordinary ductility in shear deformation, it is also necessary to investigate the model in the plastic regime, where the matrix material fails at large shear strain. To accomplish this, an ideal elasto-plastic model is considered: the

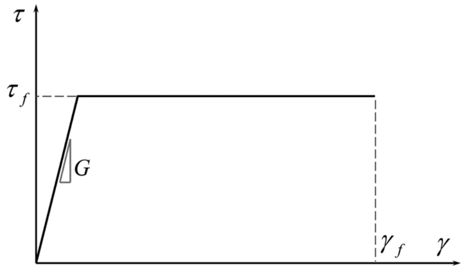

Figure 5. Ideal elastic−plastic shear model for the matrix material used in the plasticity analysis.

tablets still deform linear elastically and show brittle failure at a tensile strength of σ_f, while the matrix is modeled as an ideal elasto-plastic material, with a yield shear stress of τ_f and plastically deforming until shear failure at a shear strain of γ_f (see Figure 5). When matrix (or interface) plasticity and failure are accounted for, the elastic zone in the unit cell shrinks as shear deformation increases, and a plastic zone nucleates and grows until shear failure occurs.

Based on this matrix constitutive behavior, the shear stress and tensile stress distribution along the tablet in the unit cell will contain three zones, "elastic", "plastic", and "failed" zones, when the overlap length is long enough such that shear failure in the matrix occurs; see Figure 6. As the sliding between tablets increases, the elastic zone (with a size of L_1) shrinks and the plastic zone (with a size of L_2 at both ends) grows. However, when shear failure is accounted for, a failure zone will nucleate and then propagate to the center, trailing the plastic zone. In other words, the plastic zone has an upper limit even if the overlap length goes to infinity. Therefore, to derive a critical plastic zone size, the behavior of the composite in the plastic regime must be analyzed.

In this regime, the force equilibrium given by eq 1 still holds. In the failure zone where the shear stress drops to zero, the tensile stress remains constant. In the plastic zone where the shear stress is τ_f, the tensile stress varies linearly according to $d\sigma_1/dx = \tau_f/b$ and $d\sigma_2/dx = -\tau_f/b$. Thus, at the boundary of the left plastic zone and the elastic zone in the top tablet, the tensile stress level is given by $\sigma' = \tau_f L_2/b$. By introducing a new coordinate, x' (see Figure 6), equilibrium in the interval $0 \le x' \le L_2$ yields

$$\frac{du_1}{dx'} - \frac{du_2}{dx'} = \frac{2\sigma'}{EL_2}x' - \frac{\sigma_0}{E} \tag{13}$$

Integrating eq 13 and applying the boundary condition that $\gamma = \gamma_f$ at $x' = 0$ (onset of failure), the shear strain distribution in the plastic zone ($0 \le x' \le L_2$) is

$$\gamma(x') = \frac{\sigma'}{EhL_2}x'^2 - \frac{\sigma_0}{Eh}x' + \gamma_f \tag{14}$$

Applying the second boundary condition that $\gamma = \tau_f/G$ at $x' = L_2$ (onset of plasticity), the plastic zone size takes the form of

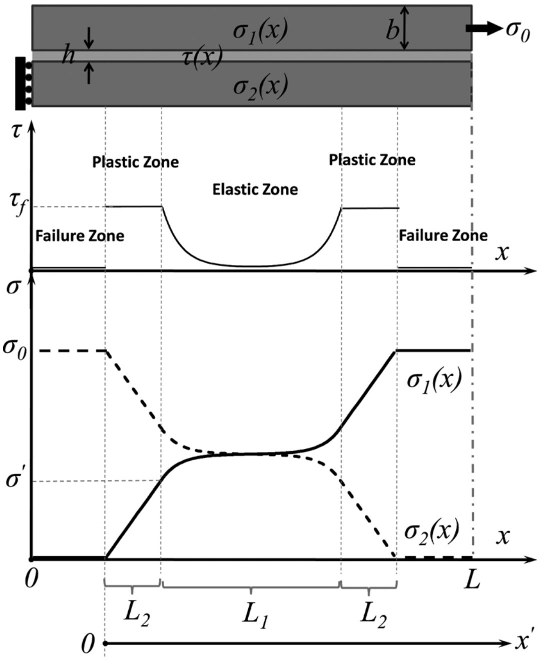

Figure 6. Typical shear stress and tensile stress distribution in the unit cell for the matrix are modeled as an ideal elastic−plastic material (overlap length is assumed long enough to allow shear failure in the matrix).

$$L_2 = \frac{Eh(G\gamma_f - \tau_f)}{G(\sigma_0 - \sigma')} \tag{15}$$

Integrating eq 1 over the plastic and elastic zones, the total applied tensile stress on the top tablet can be expressed as

$$\sigma_0 = \frac{2\tau_f}{b}\left[L_2 + \frac{1}{\lambda}\tanh\left(\frac{\lambda L_1}{2}\right)\right] \tag{16}$$

Combining eqs 15 and 16, the plastic zone size can be written as

$$L_2 = \frac{1}{\lambda}\left\{\sqrt{\frac{2(G\gamma_f - \tau_f)}{\tau_f} + \tanh^2\left(\frac{\lambda L_1}{2}\right)} - \tanh\left(\frac{\lambda L_1}{2}\right)\right\} \tag{17}$$

Substituting eq 17 back into eq 16, the tensile stress applied on the top tablet is

$$\sigma_0 = \frac{2\tau_f}{b\lambda}\sqrt{\frac{2(G\gamma_f - \tau_f)}{\tau_f} + \tanh^2\left(\frac{\lambda L_1}{2}\right)} \tag{18}$$

Note that eqs 17 and 18 are the plastic solutions assuming the tablet is strong enough (such that the tablet will not fail at the applied stress σ_0) and the overlap length is sufficiently long (such that the failure zone occurs before the elastic zone disappears). In addition, eq 18 gives the upper limit of the applied tensile stress by having the overlap length go to infinity, *i.e.*, $L_1 \to \infty$,

$$\sigma_0^{\max} = \sqrt{\frac{2Eh(2G\gamma_f - \tau_f)\tau_f}{Gb}} \tag{19}$$

In other words, no matter how long the tablet overlap is, the effective strength of the composite cannot exceed

$$\sigma_{\mathrm{eff}}{}^{\max} = \frac{b}{2b+h}\sigma_0{}^{\max} = \frac{1}{2b+h}\sqrt{\frac{2Ebh(2G\gamma_{\mathrm{f}} - \tau_{\mathrm{f}})\tau_{\mathrm{f}}}{G}} \qquad (20)$$

Furthermore, as the elastic zone disappears (*i.e.*, $L_1 \rightarrow 0$), eq 17 gives the upper limit of the plastic zone size

$$L_2{}^{\max} = \frac{1}{\lambda}\sqrt{\frac{2(G\gamma_{\mathrm{f}} - \tau_{\mathrm{f}})}{\tau_{\mathrm{f}}}} = \sqrt{\frac{Ehb(G\gamma_{\mathrm{f}} - \tau_{\mathrm{f}})}{G\tau_{\mathrm{f}}}} \qquad (21)$$

Therefore, when the tablet does not fail, a characteristic overlap length is given by

$$L^{***} = 2L_2{}^{\max} = 2\sqrt{\frac{Ehb(G\gamma_{\mathrm{f}} - \tau_{\mathrm{f}})}{G\tau_{\mathrm{f}}}} \qquad (22)$$

If the tablet strength is such that it is smaller than that resulting from the upper limit of the plastic length, $2L_2{}^{\max}$, given by eq 21, *i.e.*,

$$\sigma_{\mathrm{f}} < \frac{2L_2{}^{\max}\tau_{\mathrm{f}}}{b} = 2\sqrt{\frac{Eh(G\gamma_{\mathrm{f}} - \tau_{\mathrm{f}})\tau_{\mathrm{f}}}{Gb}} \qquad (23)$$

then another characteristic overlap length is simply obtained from the equilibrium of the unit cell, and it is given by

$$L^{**} = \frac{\sigma_{\mathrm{f}}}{\tau_{\mathrm{f}}}b \qquad (24)$$

This solution has the physical meaning that when the overlap length equals L^{**}, the tablet and interface fail simultaneously. The characteristic overlap length in eq 24 takes the identical form to that reported by Gao *et al.*[15] However, we want to emphasize the solution in eq 24 comes from a rigorous derivation and is a specific solution in the plastic regime. In other words, the characteristic overlap length L^{**}, although containing only plastic properties of the constituents, is valid when eq 23 holds, in which not only the plastic properties but also the elastic properties of constituents are accounted for.

MODEL VALIDATION AND DISCUSSION

The elastic solution discussed in the previous section provides a critical length that optimizes the total elastic strain energy density of a composite. It is worth noting that in the elastic region the length scale where the total elastic strain energy density is maximized differs from that at which the composite is optimized in strength. For a composite with a brittle interface (linear elastic shear behavior until failure), the elastic strain energy density of the material is still maximized at the characteristic length, L^*. Giving that the brittle interface fails at shear strength, τ_{f}, by rearranging eq 6 one can express the effective strength of the composite as a hyperbolic tangent function of the overlap length, namely,

$$\sigma_{\mathrm{eff}} = \frac{2\tau_{\mathrm{f}}}{(2b+h)\lambda}\tanh\left(\frac{\lambda L}{2}\right) \qquad (25)$$

This suggests that the strength of the material first monotonically increases with the overlap length and then saturates at $L \gg L^*$.

. Therefore, to optimize the composite performance in terms of both toughness and strength, the ductility of the interface material also plays an important role, as discussed in the context of the plastic solution. By tailoring the plastic properties of the interface material, the effective strength of the composite materials can be optimized in the second characteristic overlap length, L^{**}, which is usually larger than L^*. Naturally, as the properties of the interface material are tailored such that L^{**} approaches L^*, the toughness and strength of the composite are simultaneously optimized. In the following, this hypothesis is verified by comparing the model's predictions for the overlap lengths of three typical natural materials and those experimentally observed to occur in nature.

Nacre from Abalone Shell. First, the model is applied to nacre to predict the optimized overlap length of adjacent aragonite tablets. Nacre from red abalone is one of the most studied materials found in nature. Microscopy observations[19] have shown that abalone nacre consists of 0.5 μm thick single-crystal aragonite tablets overlaid on each other and connected by a 25 nm thick organic matrix. Previous statistical microscopic characterization of the overlapped length of abalone shell found an average overlap length of 1.6 μm.[11,12] The in-plane and out-of-plane elastic moduli of the single-crystal aragonite tablet have been experimentally determined to be E = 106 GPa and $E_{\perp}$ = 82 GPa, respectively.[43] The shear modulus of the organic interlayer is approximately 1.4 GPa with an average shear strength of approximately 37 MPa.[8] In addition, the organic matrix exhibits high shear ductility; the shear failure strain is about 100%.[43] The tablet strength of abalone shell has a wide distribution, due to the randomly distributed defects in the minerals.[44] The tensile strength of individual aragonite tablet has yet to be experimentally characterized. Since the aragonite mineral is brittle, we use the quasi-static compressive failure stress of nacre shells to approximate the intrinsic tablet strength. Menig *et al.*[45] performed quasi-static compressive experiments on abalone shells and reported compressive strengths ranging from 100 to 500 MPa. Here we take the strength of an aragonite tablet, σ_{f} =235 MPa, at which 50% of the specimens failed.[45] Applying the mechanical properties of the aragonite tablets and the organic matrix to our continuum model yields two characteristic overlap lengths of $L^* \approx 1.59$ μm and $L^{**} \approx 1.69$ μm, which are very consistent with the microscopy characterization

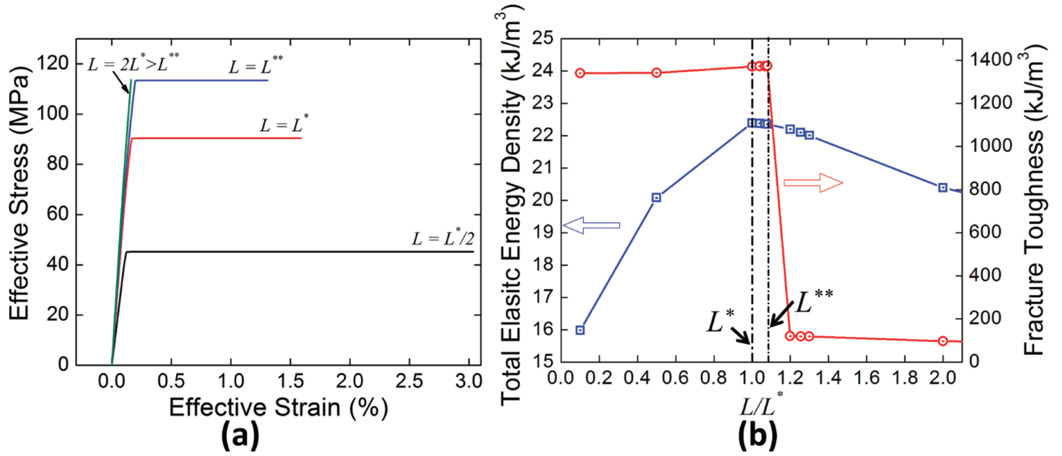

Figure 7. Finite element simulation results showing overlap length effects on the mechanical response of nacre. (a) Effective stress–strain responses for different overlap lengths. (b) Elastic and fracture toughness varying with overlap length normalized by L^*. Total elastic strain energy density (squares) maximizes at $L = L^*$, and fracture toughness (circles) exhibits a sudden drop when $L > L^{**}$.

of 1.6 μm. To demonstrate how the overlap length affects the composite's performance, finite element modeling has been performed to obtain the stress–strain responses at varying overlap lengths. Figure 7a shows the finite element simulation results of four typical effective stress–strain responses of abalone shell for overlap lengths increasing from $L^*/2$ to $2L^*$. It is clear that when the overlap length increases, the stiffness and strength of the composite improves while some ductility is sacrificed. When the overlap length approaches L^{**}, the composite enters an unstable region and the material becomes more brittle. Figure 7b summarizes the effects of overlap length on the total elastic strain energy density and the energy to failure (fracture toughness). As predicted by the continuum analysis, the total elastic strain energy density is optimized at $L = L^*$, which corresponds to the highest resistance to damage initiation. Second, the fracture toughness increases monotonically when the overlap length increases and has a sudden drop at around $L = L^{**}$. This indicates that the composite becomes very unstable when $L \geq L^{**}$ and exhibits a transition from ductile to brittle behavior.

Collagen in Tendon/Bone. Next the model is applied to predict the overlap of collagen fibrils in tendon. Experiments and atomistic calculations on tropocollagen molecules[28,46−53] reported elastic moduli ranging from 0.35 to 18 GPa. This broad distribution is probably due to the different strain rates used in the studies, as the stiffness of the tropocollagen molecule is found to be highly sensitive to strain rate and strain level.[53] At a slow stretching rate of 0.5 m/s and small strain level, the elastic modulus of the tropocollagen molecule is approximately 4 GPa.[53] The shear modulus of the cross-links in the overlap region in collagen fibrils in a wet environment is approximately 3.4 MPa, as measured by micromechanical bending experiments.[54] The diameter of a tropocollagen molecule, $2b$, is about 1.23 nm, and the gap between tropocollagen molecules, h, is about 0.24 nm.[21] Substituting the mechanical properties of the tropocollagen molecule and the transverse dimensions given above, the characteristic overlap length, L^*, is ∼31 nm, which also compares very well with the overlap length of 27 nm identified by electron microscopy 3-D reconstruction.[21]

Spider Silk. Finally, the model is applied to predict the overlap length between β-sheets in spider silk, which are an example of much smaller scale constituents than the previous two examples. β-Sheets are the building blocks for spider silk fibrils with subnanometer dimensions. At such length scales, experiments to characterize elastic properties are extremely difficult to perform. Hence, molecular dynamic simulations have been used to study the stiffness, strength, and mechanical toughness of β-sheet crystals.[31,32] Bending deformation on a β-sheet cantilever in a large-scale molecular dynamic simulation[31] reported an elastic modulus of $E = 22.6$ GPa and a shear modulus (representative of the cross-links between β-sheets) of $G = 4.6$ GPa. The shear strength of H-bonds, which defines τ_f in the model, reaches 200 MPa.[32] The thickness of a β-sheet, $2b$, is about 1 nm, and the distance between β-sheets equals the H-bond length, *i.e.*, $h \approx 0.3$ nm. Substituting the elastic properties and transversal dimensions of the β-sheet crystal reported above, the characteristic overlap length of the β-sheet, L^*, is about 2 nm. Substituting $\tau_f = 200$ MPa and assuming $\sigma_f \approx E/10 = 2.26$ GPa, the model predicts $L^{**} \approx 5.7$ nm. As the periodic distance of H-bonds is about 0.75 nm, an overlap length between L^* and L^{**} implies that the optimized number of H-bonds in β-sheet crystals is 3–8. This agrees very well with the experimental data of β-sheet length, which ranges from 2 to 8 nm.[55] Likewise, a large-scale molecular dynamic simulation suggests that the shear strength between β-sheets is optimized at a critical cluster size of 3–4 H-bonds.[32]

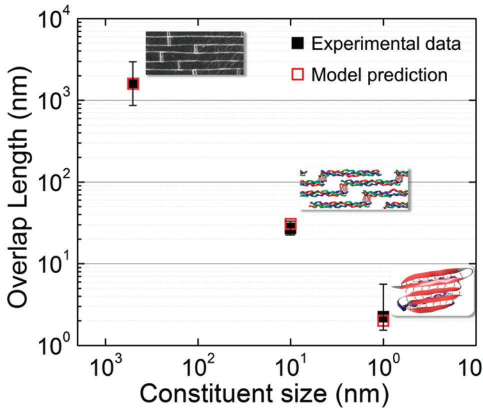

Figure 8. Comparison of overlap lengths for basic building blocks of three natural materials (nacre, tendon, and spider silk) from experimental observation (solid squares) and model prediction (open squares).

Through application of the model to predict the optimized overlap lengths for three typical natural materials, at length scales that range from micrometer to nanometer, we have found very good agreement with the experimentally observed geometries. The results are summarized in Figure 8. This suggests that the numerical model provides not just a simply solution for a specific material but a general criterion for composite material design.

Model Application to Carbon-Based Composites Design. In this section, the application of the model to the design of novel carbon-based composite materials is discussed. As will be demonstrated here, the model predictions can serve as the basis for the development of lightweight materials with enhanced mechanical properties such as high specific strength and toughness. Figure 9a shows the biomimic hierarchical structure of a CNT yarn, in which aligned CNTs interact with each other *via* van der Waals (vdW) interactions or through cross-linking polymers.[38,56,57] As a first study, the model is applied on a pristine yarn where shear through vdW interactions between CNTs is assumed as the only load transfer mechanism (*i.e.*, no cross-linking polymer between CNTs). The representative unit containing two bare multiwall carbon nanotubes (MWCNTs) is shown in Figure 9b. In addition, since the reinforcement (MWCNT) has a circular cross-section, the continuum model introduced above is next modified accordingly.

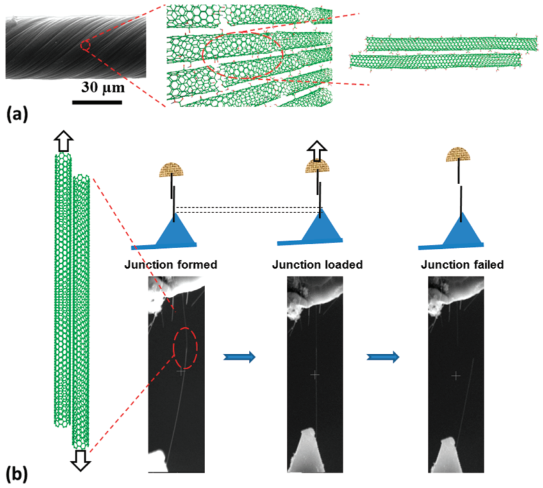

Figure 9. (a) Hierarchical structure of CNT yarns. SEM image of a CNT yarn with a diameter of about 30 μm and schematics showing the interaction between functionalized CNTs through shear (green, red, and gray atoms represent carbon, oxygen, and hydrogen atoms, respectively). (b) Procedure of *in situ* shear experiment on pristine CNTs in SEM.

Assuming the cross-section of the MWCNTs remains circular during deformation and only the outer shell of each MWCNT carries the tensile load,[58] the force equilibrium condition, eq 1, can be rewritten as

$$w_{\mathrm{eff}}\tau(x) = \frac{\mathrm{d}\sigma_1(x)}{\mathrm{d}x}\pi\varphi\delta = \frac{\mathrm{d}\sigma_2(x)}{\mathrm{d}x}\pi\varphi\delta \qquad (26)$$

in which ϕ is the MWCNT outer diameter, δ is the shell spacing (0.34 nm), and w_{eff} is the effective contact width of two MWCNTs. In this case, the first characteristic overlap length is given by

$$L^* = 2.318\sqrt{\frac{Eh}{\tilde{G}}\left(\frac{\pi\varphi\delta}{w_{\mathrm{eff}}}\right)} \qquad (27)$$

where $\tilde{G}$ is the effective shear modulus of the interface with the circular cross-section accounted for. Similarly, eq 25 can be recasted as

$$F = \frac{2\tau_f w_{\mathrm{eff}}}{\lambda}\tanh\left(\frac{\lambda L}{2}\right) \text{ and } \lambda = \sqrt{\frac{2\tilde{G}}{Eh}\left(\frac{w_{\mathrm{eff}}}{\pi\varphi\delta}\right)} \qquad (28)$$

,where F is the maximum shear force beyond which the MWCNT junction in the unit cell starts to slide and fail. As suggested by the hyperbolic function in eq 28, the shear force increases linearly when overlap length is small and saturates at a very large overlap length.

To assess the model capabilities, *in situ* shear experiments were performed on unfunctionalized MWCNTs inside a scanning electron microscope (SEM) as shown in Figure 9b. In this way, the maximum shear force to break the junctions between the two MWCNTs was characterized as a function of overlap length (see Figure 10a). Model predictions using the parameters described in the following paragraphs, with lower and upper bonds of shear strength of 30 and 60 MPa, describe the experimental data quite well. Initially the junction failure force increases linearly with overlap length and then starts to saturate at approximately 400 nm. This indicates the experimental results might contain the material's intrinsic mechanical properties, such as shear strength; see eq 28. Interestingly, the experimental data fell into the region in between the two curves with shear strengths of 30 and 60 MPa for armchair and zigzag tubes, respectively (Figure 10a). This suggests that the shear between two MWCNTs is

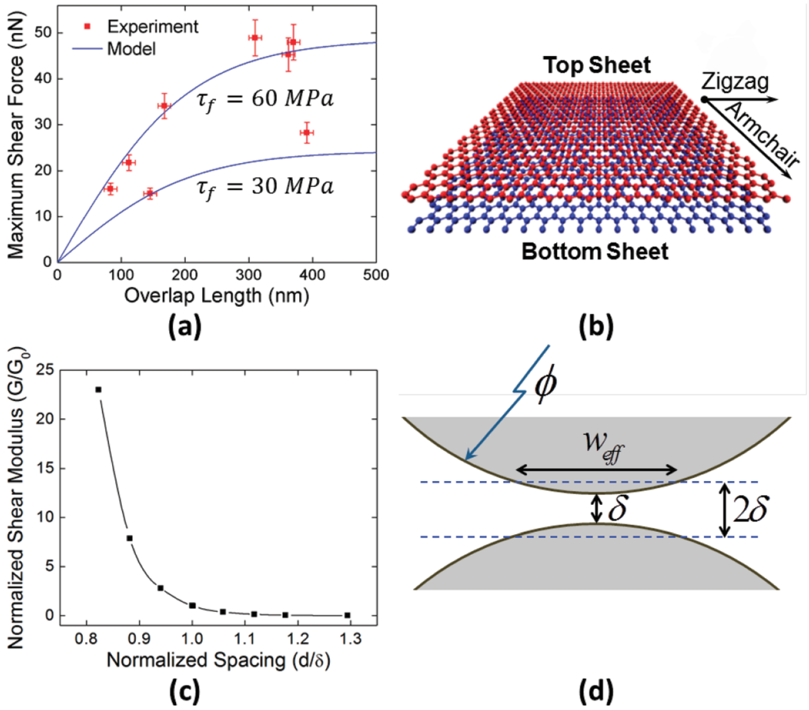

Figure 10. (a) Experimental results for *in situ* SEM shear tests for unfunctinalized MWCNTs. In addition, model predictions yield the lower and upper bonds of shear strength, 30 and 60 MPa, respectively. (b) Schematic of the bilayer graphene used in the MD calculations. (c) MD results show that the out-of-plane shear modulus of graphene sheets follows an inverse power law relationship with the sheet spacing. (d) Cross-section view of two adjacent MWCNTs and criterion to define the effective contact width.

dependent on chirality, which is verified by the atomistic calculations discussed below.

Transmission electron microscope (TEM) studies have shown that the MWCNTs used in this study have an average outer diameter, ϕ, of ~23 nm and inner diameter of about 10 nm. The minimum spacing between two MWCNTs at equilibrium is approximately identical to the shell spacing; $\delta = 0.34$ nm. As shown in Figure 10d, the effective contact width, w_{eff}, is defined as the width within which the gap between two MWCNTs is less than or equal to 2δ. Thus, $w_{\text{eff}} = (\phi^2 - (\phi - \delta)^2)^{1/2}$. To estimate the shear modulus of the interface, molecular mechanics (MM) calculations were performed between two graphene sheets. The open source code LAMMPS (large scale atomistic/molecular massively parallel simulator,[57,59]) was used with the AIREBO potential[60] to account for both covalent bonds and vdW interactions between carbon atoms. As shown in Figure 10b, two graphene sheets, with a size of approximately 5×5 nm^2, were first relaxed at 0 K to the equilibrium state. Then the bottom graphene sheet was fixed while the shear displacement was prescribed on the top sheet. The simulation box size was approximately $5 \times 5 \times 20$ nm^3, and periodic boundary conditions were used. To account for anisotropy, the top sheet was displaced along the zigzag and armchair directions, respectively. The shear strain was computed as the ratio between the sliding distance and the equilibrium spacing of 0.34 nm. The shear stress was computed as the total force acting on the top sheet divided by the area. The MM simulations suggest that the out-of-plane shear modulus of bilayer graphene sheets ranges from 0.2 to 0.5 GPa depending on the shear directions. Furthermore, the MM simulations suggest that the shear strength between two graphene sheets is dependent on the shear directions. Shearing in the armchair direction yields a shear strength of 58 MPa, and shearing in the zigzag direction yields a shear strength of 28 MPa. Additional MM simulations were done to investigate the shear modulus dependence on the spacing between two graphene sheets. Results show that the shear modulus decreases as a power law function of spacing (see Figure 10c), namely,

$$G = G_0 \left(\frac{d}{\delta}\right)^{-16.14} \qquad (29)$$

in which G is the out-of-plane shear modulus at an intershell spacing of d, and G_0 is the out-of-plane shear modulus at equilibrium spacing $\delta = 0.34$ nm. Equation 29 provides a way to estimate the effective shear modulus, $\tilde{G}$, over the effective contact width for the two MWCNTs. Integrating eq 29 yields an effective shear modulus $\tilde{G} \approx 0.1$ GPa. Given the tensile modulus of CNT, $E = 1$ TPa, and $h = \delta = 0.34$ nm, the shear strength, τ_f, is the only free parameter in eq 28. Applying the numerical model, it is found that the experimental data fall in between the two curves where shear strengths of 30 and 60 MPa were used. These two limits of the shear strength agree with those obtained from MM simulations very well and imply that the MWCNTs used in this study contain random chiral angles. The shear strength measured here is in the range of previously reported values.[61−64] It is worth noting that in previous reports the shear stress was simply defined as the total shear force divided by the whole overlap area. This could be the reason that previously reported shear strength of unfunctionalized CNTs shows a significant scatter. Our analysis differs from previous ones by considering the distribution of the shear stress over the overlap region. In this way, the value reported in this study could be treated as a material's intrinsic property.

Inputting the material properties in eq 27 yields the first characteristic overlap length, L^*, of approximately 300 nm. As the vdW interaction between pristine CNTs is very weak, eq 28 suggests that for perfectly overlapped CNTs the maximum shear force will reach a plateau when the overlap length increases. In other words, the junctions between CNTs tend to fail by sliding before MWCNT fracture, indicating the second characteristic overlap length, L^{**}, is infinitely large. One approach to improve the interactions between tubes is changing the morphology of the overlapped CNTs, such as introducing wrapping between CNTs by twisting.[39] However, large twisting angles could lead to performance degradation. Therefore, functionalizing the CNTs with polymers possessing the right chemical bonds and chain flexibility (molecular weight) can lead to improved shear interactions. The model provides insight into characteristics desirable in these novel polymers. Their shear strength and ductility should be such that L^{**} can be brought close to L^*. Such optimized interface behavior can be achieved by choosing the right functional groups. For example, one can envision carboxylic groups (short chains: H-bond acceptors and donors), propanoic/butanoic acid groups (longer chains: H-bond acceptors and donors), and para-aramide groups (Kevlar: combination of π-stacking and H-bonds) as promising functional groups. In this regard, the *in situ* SEM shear experiment can serve as an efficient tool to quantitatively investigate interface properties leading to optimal performance for a given constituent elasticity and strength. Together with atomistic calculations, the shear experiment can provide the necessary information for the model here presented to guide the geometric design of high-performance carbon-based (*e.g.*, CNT and graphene) composites.

CONCLUSION

In this study, a continuum model has been derived by rigorously solving the shear-lag model analytically in both elastic and plastic regimes. The model connects the effective mechanical properties of composite materials to the mechanical behavior of discontinuous reinforcements, their geometry, and chemistry of cross-links governing lateral interactions. The model reveals that optimal mechanical performance (simultaneous high toughness and strength) is a strong function of overlap length in the discontinuous reinforcement-matrix architecture. More importantly, it provides a mathematical framework for understanding synergistic effects. In this context, characteristic overlap lengths are identified and shown to be dependent on the properties of the reinforcement material and chemistry of the cross-linking molecules (bond type and density). In addition, it is shown that the ductility of the matrix in shear deformation, as controlled by such molecules, plays an important role in the composite's overall ductility. The model is presented in a 2-D framework and, as such, is complementary to prior investigations of 3-D effects in natural materials, *e.g.*, nacre,[6,11,12,14,16,18−20,43] in which the 3-D architecture implies a more complex behavior leading to simultaneous high stiffness and toughness.

Validated by successfully predicting the characteristic overlap lengths in three well-known natural composites, with differing geometries that scale from micrometer down to nanometer levels, the model serves as a guideline in designing novel composite materials. Furthermore, *in situ* shear experiments on pristine MWCNTs confirm the numerical model capability to describe load transfer between constituents. In the future, the shear experiment and numerical model introduced in this study can serve as valuable tools for designing high-performance carbon-based nanocomposites.

METHODS

MWCNTs grown with an arc discharge method (provided by n-Tec) were used in *in situ* SEM shear experiments. X-ray photoelectron spectroscopy studies (not presented here) confirm no appreciable noncarbonaceous impurities, justifying the assumption of pure vdW interactions between MWNTs. As shown in Figure 9b, one of the two MWCNTs is mounted on a calibrated atomic force microscope (AFM) cantilever whose spring constant is known. The other MWCNT is attached on a three-axis actuator, through which the two MWCNTs can be brought together to form a junction *in situ* in the SEM. The junction length was varied in the range 50 to 400 nm. To shear the junction, the actuator was moved away from the AFM cantilever until the junction failed. The maximum shear load at failure was obtained by recording the AFM cantilever deflection.

Conflict of Interest: The authors declare no competing financial interest.

Acknowledgment. The authors acknowledge the support of ARO through MURI Award No. W911NF-08-1-0541 and ONR through Award No. N00014-08-1-1055. The authors acknowledge

Mr. Zhi An for XPS characterization of MWCNTs and Dr. Shuyou Li for TEM imaging of MWCNTs.

REFERENCES AND NOTES

1. Ashby, M.; Gibson, L.; Wegst, U.; Olive, R. The Mechanical Properties of Natural Materials. I. Material Property Charts. *Proc. R. Soc. London A: Math. Phys. Sci.* **1995**, *450*, 123–140.
2. Fratzl, P.; Gupta, H.; Paschalis, E.; Roschger, P. Structure and Mechanical Quality of the Collagen–Mineral Nano-Composite in Bone. *J. Mater. Chem.* **2004**, *14*, 2115–2123.
3. Launey, M. E.; Ritchie, R. O. On the Fracture Toughness of Advanced Materials. *Adv. Mater.* **2009**, *21*, 2103–2110.
4. Launey, M. E.; Munch, E.; Alsem, D. H.; Barth, H.; Saiz, E.; Tomsia, A. P.; Ritchie, R. O. Designing Highly Toughened Hybrid Composites through Nature-Inspired Hierarchical Complexity. *Acta Mater.* **2009**, *57*, 2919–2932.
5. Currey, J.; Taylor, J. The Mechanical Behaviour of Some Molluscan Hard Tissues. *J. Zool.* **1974**, *173*, 395–406.
6. Espinosa, H. D.; Rim, J. E.; Barthelat, F.; Buehler, M. J. Merger of Structure and Material in Nacre and Bone-Perspectives on De Novo Biomimetic Materials. *Prog. Mater. Sci.* **2009**, *54*, 1059–1100.
7. Lin, A. Y. M.; Meyers, M. A.; Vecchio, K. S. Mechanical Properties and Structure of Strombus Gigas, Tridacna Gigas, and Haliotis Rufescens Sea Shells: A Comparative Study. *Mater. Sci. Eng., C* **2006**, *26*, 1380–1389.
8. Jackson, A.; Vincent, J.; Turner, R. The Mechanical Design of Nacre. *Proc. R. Soc. London B: Biol. Sci.* **1988**, *234*, 415–440.
9. Barthelat, F.; Espinosa, H. An Experimental Investigation of Deformation and Fracture of Nacre–Mother of Pearl. *Exp. Mech.* **2007**, *47*, 311–324.
10. Kotha, S.; Li, Y.; Guzelsu, N. Micromechanical Model of Nacre Tested in Tension. *J. Mater. Sci.* **2001**, *36*, 2001–2007.
11. Espinosa, H. D.; Juster, A. L.; Latourte, F. J.; Loh, O. Y.; Gregoire, D.; Zavattieri, P. D. Tablet-Level Origin of Toughening in Abalone Shells and Translation to Synthetic Composite Materials. *Nat. Commun.* **2011**, *2*, 173.
12. Barthelat, F.; Tang, H.; Zavattieri, P.; Li, C. M.; Espinosa, H. On the Mechanics of Mother-of-Pearl: A Key Feature in the Material Hierarchical Structure. *J. Mech. Phys. Solids* **2007**, *55*, 306–337.
13. Munch, E.; Launey, M. E.; Alsem, D. H.; Saiz, E.; Tomsia, A. P.; Ritchie, R. O. Tough, Bio-Inspired Hybrid Materials. *Science* **2008**, *322*, 1516.
14. Bonderer, L. J.; Studart, A. R.; Gauckler, L. J. Bioinspired Design and Assembly of Platelet Reinforced Polymer Films. *Science* **2008**, *319*, 1069–1073.
15. Gao, H.; Ji, B.; Jäger, I.; Arzt, E.; Fratzl, P. Materials Become Insensitive to Flaws at Nanoscale: Lessons from Nature. *Proc. Natl. Acad. Sci. U. S. A.* **2003**, *100*, 5597.
16. Wang, R.; Suo, Z.; Evans, A.; Yao, N.; Aksay, I. Deformation Mechanisms in Nacre. *J. Mater. Res.* **2001**, *16*, 2486.
17. Evans, A.; Suo, Z.; Wang, R.; Aksay, I.; He, M.; Hutchinson, J. Model for the Robust Mechanical Behavior of Nacre. *J. Mater. Res.* **2001**, *16*, 2476.
18. Song, F.; Soh, A.; Bai, Y. Structural and Mechanical Properties of the Organic Matrix Layers of Nacre. *Biomaterials* **2003**, *24*, 3623–3631.
19. Meyers, M.; Lin, A.; Chen, P.; Muyco, J. Mechanical Strength of Abalone Nacre: Role of the Soft Organic Layer. *J. Mech. Behav. Biomed. Mater.* **2008**, *1*, 76–85.
20. Katti, K. S.; Katti, D. R.; Pradhan, S. M.; Bhosle, A. Platelet Interlocks Are the Key to Toughness and Strength in Nacre. *J. Mater. Res.* **2005**, *20*, 1097–1100.
21. Landis, W.; Song, M.; Leith, A.; McEwen, L.; McEwen, B. Mineral and Organic Matrix Interaction in Normally Calcifying Tendon Visualized in Three Dimensions by High-Voltage Electron Microscopic Tomography and Graphic Image Reconstruction. *J. Struct. Biol.* **1993**, *110*, 39–54.
22. Fratzl, P. Cellulose and Collagen: From Fibres to Tissues. *Curr. Opin. Colloid Interface Sci.* **2003**, *8*, 32–39.
23. Fratzl, P.; Weinkamer, R. Nature's Hierarchical Materials. *Prog. Mater. Sci.* **2007**, *52*, 1263–1334.
24. Lakes, R. Materials with Structural Hierarchy. *Nature* **1993**, *361*, 511–515.
25. van der Rijt, J. A. J.; van der Werf, K. O.; Bennink, M. L.; Dijkstra, P. J.; Feijen, J. Micromechanical Testing of Individual Collagen Fibrils. *Macromol. Biosci.* **2006**, *6*, 697–702.
26. Shen, Z. L.; Dodge, M. R.; Kahn, H.; Ballarini, R.; Eppell, S. J. Stress-Strain Experiments on Individual Collagen Fibrils. *Biophys. J.* **2008**, *95*, 3956–3963.
27. Shen, Z. L.; Dodge, M. R.; Kahn, H.; Ballarini, R.; Eppell, S. J. In Vitro Fracture Testing of Submicron Diameter Collagen Fibril Specimens. *Biophys. J.* **2010**, *99*, 1986–1995.
28. Buehler, M. Atomistic and Continuum Modeling of Mechanical Properties of Collagen: Elasticity, Fracture, and Self-Assembly. *J. Mater. Res.* **2006**, *21*, 1947–1961.
29. Buehler, M. J. Molecular Architecture of Collagen Fibrils: A Critical Length Scale for Tough Fibrils. *Curr. Appl. Phys.* **2008**, *8*, 440–442.
30. Vollrath, F.; Knight, D. P. Liquid Crystalline Spinning of Spider Silk. *Nature* **2001**, *410*, 541–548.
31. Keten, S.; Xu, Z.; Ihle, B.; Buehler, M. J. Nanoconfinement Controls Stiffness, Strength and Mechanical Toughness of β-Sheet Crystals in Silk. *Nat. Mater.* **2010**, *9*, 359–367.
32. Keten, S.; Buehler, M. J. Asymptotic Strength Limit of Hydrogen-Bond Assemblies in Proteins at Vanishing Pulling Rates. *Phys. Rev. Lett.* **2008**, *100*, 198301.
33. Lee, C.; Wei, X.; Kysar, J. W.; Hone, J. Measurement of the Elastic Properties and Intrinsic Strength of Monolayer Graphene. *Science* **2008**, *321*, 385.
34. Peng, B.; Locascio, M.; Zapol, P.; Li, S.; Mielke, S. L.; Schatz, G. C.; Espinosa, H. D. Measurements of near-Ultimate Strength for Multiwalled Carbon Nanotubes and Irradiation-Induced Crosslinking Improvements. *Nat. Nanotechnol.* **2008**, *3*, 626–631.
35. Ajayan, P.; Stephan, O.; Colliex, C.; Trauth, D. Aligned Carbon Nanotube Arrays Formed by Cutting a Polymer Resin--Nanotube Composite. *Science* **1994**, *265*, 1212.
36. Dalton, A. B.; Collins, S.; Munoz, E.; Razal, J. M.; Ebron, V. H.; Ferraris, J. P.; Coleman, J. N.; Kim, B. G.; Baughman, R. H. Super-Tough Carbon-Nanotube Fibres. *Nature* **2003**, *423*, 703–703.
37. Harris, P. Carbon Nanotube Composites. *Int. Mater. Rev.* **2004**, *49*, 31–43.
38. Koziol, K.; Vilatela, J.; Moisala, A.; Motta, M.; Cunniff, P.; Sennett, M.; Windle, A. High-Performance Carbon Nanotube Fiber. *Science* **2007**, *318*, 1892–1895.
39. Liu, K.; Sun, Y.; Zhou, R.; Zhu, H.; Wang, J.; Liu, L.; Fan, S.; Jiang, K. Carbon Nanotube Yarns with High Tensile Strength Made by a Twisting and Shrinking Method. *Nanotechnology* **2010**, *21*, 045708.
40. Naraghi, M.; Filleter, T.; Moravsky, A.; Locascio, M.; Loutfy, R. O.; Espinosa, H. D.; Multiscale, A Study of High Performance Double-Walled Nanotube- Polymer Fibers. *ACS Nano* **2010**, 2212–2215.
41. Cox, H. The Elasticity and Strength of Paper and Other Fibrous Materials. *Br. J. Appl. Phys.* **1952**, *3*, 72.
42. Chen, B.; Wu, P.; Gao, H. A Characteristic Length for Stress Transfer in the Nanostructure of Biological Composites. *Compos. Sci. Technol.* **2009**, *69*, 1160–1164.
43. Tang, H.; Barthelat, F.; Espinosa, H. An Elasto-Viscoplastic Interface Model for Investigating the Constitutive Behavior of Nacre. *J. Mech. Phys. Solids* **2007**, *55*, 1410–1438.
44. Suk, J. W.; Piner, R. D.; An, J.; Ruoff, R. S. Mechanical Properties of Monolayer Graphene Oxide. *ACS Nano* **2010**, 351–355.
45. Menig, R.; Meyers, M.; Meyers, M.; Vecchio, K. Quasi-Static and Dynamic Mechanical Response of Haliotis Rufescens (Abalone) Shells. *Acta Mater.* **2000**, *48*, 2383–2398.
46. Harley, R.; James, D.; Miller, A.; White, J. Phonons and the Elastic Moduli of Collagen and Muscle. *Nature* **1977**, *267*, 285–287.
47. Cusack, S.; Miller, A. Determination of the Elastic Constants of Collagen by Brillouin Light Scattering. *J. Mol. Biol.* **1979**, *135*, 39–51.
48. Hofmann, H.; Voss, T.; Kühn, K.; Engel, J. Localization of Flexible Sites in Thread-Like Molecules from Electron

Micrographs:: Comparison of Interstitial, Basement Membrane and Intima Collagens. *J. Mol. Biol.* **1984**, *172*, 325–343.

49. Sasaki, N.; Odajima, S. Stress-Strain Curve and Young's Modulus of a Collagen Molecule as Determined by the X-Ray Diffraction Technique. *J. Biomech.* **1996**, *29*, 655–658.
50. Sun, Y. L.; Luo, Z. P.; Fertala, A.; An, K. N. Stretching Type Ii Collagen with Optical Tweezers. *J. Biomech.* **2004**, *37*, 1665–1669.
51. Lorenzo, A. C.; Caffarena, E. R. Elastic Properties, Young's Modulus Determination and Structural Stability of the Tropocollagen Molecule: A Computational Study by Steered Molecular Dynamics. *J. Biomech.* **2005**, *38*, 1527–1533.
52. Vesentini, S.; Fitié, C. F. C.; Montevecchi, F. M.; Redaelli, A. Molecular Assessment of the Elastic Properties of Collagen-Like Homotrimer Sequences. *Biomech. Model. Mechanobiol.* **2005**, *3*, 224–234.
53. Gautieri, A.; Buehler, M. J.; Redaelli, A. Deformation Rate Controls Elasticity and Unfolding Pathway of Single Tropocollagen Molecules. *J. Mech. Behav. Biomed. Mater.* **2009**, *2*, 130–137.
54. Yang, L.; Van Der Werf, K. O.; Fitié, C. F. C.; Bennink, M. L.; Dijkstra, P. J.; Feijen, J. Mechanical Properties of Native and Cross-Linked Type I Collagen Fibrils. *Biophys. J.* **2008**, *94*, 2204–2211.
55. Penel, S.; Morrison, R. G.; Dobson, P. D.; Mortishire Smith, R. J.; Doig, A. J. Length Preferences and Periodicity in Strands. Antiparallel Edge Sheets Are More Likely to Finish in Non Hydrogen Bonded Rings. *Protein Eng.* **2003**, *16*, 957.
56. Naraghi, M.; Filleter, T.; Moravsky, A.; Locascio, M.; Loutfy, R. O.; Espinosa, H. D. Multiscale A Study of High Performance Double-Walled Nanotube-Polymer Fibers. *ACS Nano* **2010**, *4*, 6463–6476.
57. Zhang, M.; Atkinson, K. R.; Baughman, R. H. Multifunctional Carbon Nanotube Yarns by Downsizing an Ancient Technology. *Science* **2004**, *306*, 1358–1361.
58. Peng, B.; Locascio, M.; Zapol, P.; Li, S.; Mielke, S. L.; Schatz, G. C.; Espinosa, H. D. Measurements of near-Ultimate Strength for Multiwalled Carbon Nanotubes and Irradiation-Induced Crosslinking Improvements. *Nat. Nanotechnol.* **2008**, *3*, 626–631.
59. Plimpton, S. J. Fast Parallel Algorithms for Short-Range Molecular Dynamics. *J. Comput. Phys.* **1995**, *117*, 1–19.
60. Stuart, S.; Tutein, A.; Harrison, J. A Reactive Potential for Hydrocarbons with Intermolecular Interactions. *J. Chem. Phys.* **2000**, *112*, 6472.
61. Bhushan, B.; Ling, X.; Jungen, A.; Hierold, C. Adhesion and Friction of a Multiwalled Carbon Nanotube Sliding against Single-Walled Carbon Nanotube. *.Phys. Rev. B* **2008**, *77*.
62. Yu, M. F.; Yakobson, B. I.; Ruoff, R. S. Controlled Sliding and Pullout of Nested Shells in Individual Multiwalled Carbon Nanotubes. *J. Phys. Chem. B* **2000**, *104*, 8764–8767.
63. Suekane, O.; Nagataki, A.; Mori, H.; Nakayama, Y. Static Friction Force of Carbon Nanotube Surfaces. *Appl. Phys. Express* **2008**, *1*.
64. Cornwell, C. F.; Majure, D.; Haskins, R.; Lee, N. J.; Ebeling, R.; Maier, R.; Marsh, C.; Bednar, A.; Kirgan, R.; Welch, C. R. Critical Carbon Nanotube Length in Fibers. *Proc. Hpcmp Users Group Conf.* **2008**, 180–186.